Dendritic flux avalanches in superconducting films

V.V. Yurchenko[1], T.H. Johansen[1,2], and Y.M. Galperin[1,3]

[1]*Department of Physics and Centre for Materials Science and Nanotechnology, University of Oslo*
P.O. Box 1048, Blindern, 0316 Oslo, Norway
E-mail: Vitaliy.Yurchenko@smn.uio.no

[2]*Institute for Superconducting and Electronic Materials, University of Wollongong, NSW, Australia*

[3]*A.F. Ioffe Physico-Technical Institute, St Petersburg 194021, Russia*

Thermomagnetic instability in general, and dendritic flux avalanches in particular, have attracted considerable attention of both scientists and engineers working on superconductor applications. Though being harmful for the performance of many superconducting devices, the avalanches provide a fruitful playground for experimental and theoretical studies of complex dynamics of the vortex matter. In this paper, we report on the progress in understanding the mechanisms responsible for the development of the giant magnetic avalanches. We review recent results on magneto-optical imaging of the fingering instability in superconducting films and analyze them basing on the recent theoretical model that establishes criteria for onset of the dendritic avalanches.

1. Introduction

1.1. Vortex pinning and motion

One of the characteristic features of superconductors is perfect diamagnetism or expulsion of a weak external magnetic field, H, from their interior, the so-called Meissner and Ochsenfeld effect. In type-II superconductors, the perfect diamagnetism exists for applied fields below a lower critical field, H_{c1}, and there is a broad domain of magnetic fields, $H_{c1} \leq H \leq H_{c2}$, where the field penetrates into the sample in a form of quantized flux lines. In a perfect sample these lines-vortices form an *Abrikosov lattice* [1]. Above the upper critical field, H_{c2}, the bulk superconductivity seizes to exist. An isolated vortex consists of a *core* where the superconducting order parameter is suppressed, while the magnetic field reaches a local maximum. The radius of the core is of the order of the *coherence length*, ξ. The magnetic field outside the core decays exponentially over a distance of a magnetic penetration depth λ, where also electrical current circulates around the core. Each vortex carries one flux quantum $\Phi_0 = h/2e \approx 2.07 \cdot 10^{-15}$ Wb. The magnetic field is sup-ported by circular currents around the core. The flux lines repel each other, an interaction that can be understood applying the Ampere's law to the circular currents. This repulsion leads to a formation of a flux line lattice, most typically a hexagonal and in some cases square. A number of phases and dynamic effects in the flux line lattice was reviewed in Refs. 2, 3.

The vortices interact with a transport current via the Lorentz force per unit length

$$\mathbf{f} = \Phi_0 \left[\mathbf{j} \times \mathbf{n} \right],$$

where $\mathbf{j}$ is the current density and $\mathbf{n}$ is the unit vector along the flux line. Since the vortex motion implies moving of normal cores it is accompanied with dissipation, which is proportional to the velocity. This dissipation can be described by an effective viscosity, and the velocity is determined by the balance between the Lorentz force and the viscous force. Therefore a free vortex lattice would move as a whole with a constant velocity resulting in a finite resistance of the sample.

Fortunately, in all real superconductors the flux lines interact with material defects that act as pinning sites and

hamper their motion. Besides the pinning barriers that arise from rather inevitable structural irregularities such as vacancies, dislocations, grain boundaries, etc., there exists a rich zoo of artificially introduced pinning sites like magnetic inclusions, phases of weaker (stronger) superconductivity, lithographically patterned «antidots», magnetic dots, etc. According to the particular nature and dimensionality of the defects the pinning potential has different spatial extent, magnetic field and temperature dependencies, see Ref. 4 for a review. When a superconductor is exposed to an increasing magnetic field (or self field of a transport current), vortices are formed at the edges and then propagate inwards. The presence of pinning leads to formation of an inhomogeneous distribution of the magnetic flux. According to the *critical state model* [5] the stationary distribution can be found from Ampere's law with the condition that the current density at each point is equal to its local critical value, $j_c(\mathbf{B}, T)$, i.e.,

$$\nabla \times \mathbf{B} = \mu_0 \mathbf{j}, \quad |\mathbf{j}| = j_c(\mathbf{B}, T).$$

The case where j_c is independent on magnetic field is called the Bean model [5]. The critical current density is in practice a key measure of the applicability of superconductors since j_c is the maximum current density in a material for transport without energy loss. Microscopic evaluation of the critical current requires direct summation of vortex–vortex interactions and all elementary pinning forces, which all together is a rather unfeasible task. Therefore the critical state model has become a major paradigm in the studies of electromagnetic properties of type-II superconductors.

The critical state emerging from the balance between the Lorentz and the pinning forces is metastable. Even a slow increase in the external magnetic field may lead to total collapse of the critical state and sudden large-scale redistribution of the flux. Such dramatic events observed experimentally as abrupt drops in the magnetization are ascribed to a thermomagnetic instability where the local heat dissipation associated with vortex motion reduces the pinning, which in turn facilitates further vortex motion. With this positive feedback, a small perturbation can quickly evolve into a flux avalanche [6–19].

1.2. Experimental methods

Experimental techniques used to investigate the avalanches in the vortex matter are conventionally subdivided in two groups: *integral* and *spatially resolved*. The former one includes all types of magnetometry: inductive coils, vibrating sample magnetometry, SQUID magnetometry [20]. These methods are sensitive to global redistributions of the flux, current flow, and the resulting change in the total magnetic moment caused by an avalanche in the sample. A drawback of the integral methods

is a lack of detailed information about the jumps, their location in the sample, their morphology, etc. Moreover, the relatively low sampling rate in these methods prevents identification of jumps occurring with short time intervals. Obviously there is no chance to separate simultaneous avalanches. Thus, measurement of the volume averaged magnetization excludes a possibility to study detailed statistics of flux jumps. Yet another disadvantage is that it is impossible also to discriminate between small jumps and instrument noise. These problems are partly solved in locally resolved magnetometry, an overview of available methods can be found elsewhere [21]. One of the most powerful tools is magneto-optical imaging (MOI), which combines high magneto-spatial resolution and short acquisition times (restrained only by the exposure time of a camera). This makes MOI the most suitable real-time technique for investigation of flux avalanches.

In our experiments we use MOI based on the Faraday effect where the sensing element is an in-plane magnetized ferrite garnet film with strong Faraday rotation. The film, which is grown separately on a transparent gadolinium gallium garnet substrate, is placed directly on the top of the sample under investigation. Stray fields from the magnetic flux pattern of the sample locally remagnetize the indicator, and when shining polarized light through the film, the out-of-plane component of magnetization induces Faraday rotation. The effect is doubled after the reflected light (either from the mirror layer or, in more rare cases, from the sample surface) passes through the garnet film again. Figure 1 illustrates the principal experimental scheme. An analyzer set at 90° relative to the polarizer filters out the nonrotated light. The rotation angle, θ, is a monotonous function of the local magnetic field, *B*.

The transmitted light is projected on the matrix of a CCD camera, its intensity, *I*, being related to the rotation angle according to Malus' law

$$I = I_o \sin^2 [\theta(B) + \alpha].$$

Here α is an offset angle (equal to 0 when the polarizer and the analyzer are crossed). The dependence $\theta(B)$ can be determined by a proper calibration of the indicator film. Using this dependence together with Malus' law one can recalculate the distribution of the magnetic field in the sample from the intensity map of the projected light.

Since MOI was invented in the 1950s several materials have been used as indicator films [22]. The MOI results reported in the present paper were obtained utilizing in-plane magnetized garnet films $(Lu,Bi)_3(Fe,Ga)_5O_{12}$, grown as a few micron thick epitaxial layer on gadolinium gallium garnet (transparent) substrates. One limitation of these indicator films is a relatively small magnetic
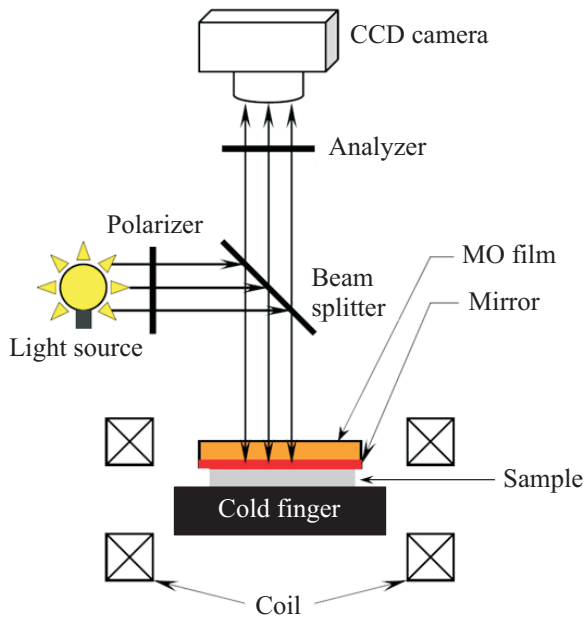
Fig. 1. Schematic draft of a MOI setup. A sample is mounted on a massive cold finger of a He-flow cryostat. Resistive coils are used as a source of an external magnetic field. The light from a mercury lamp shines through a polarizer and is guided onto an indicator film, where it experiences the Faraday rotation. The light becomes reflected by a thin mirror and projected through an analyzer on a CCD matrix of a computer-operated camera.

field range: above $\simeq 100$ mT the films reach saturation, i.e., they become magnetized totally out-of-plane.

2. Dendritic flux avalanches

Thermomagnetic instabilities have been in focus of many experimental and theoretical studies for decades [11,23]. However, only with the use of MOI it has been
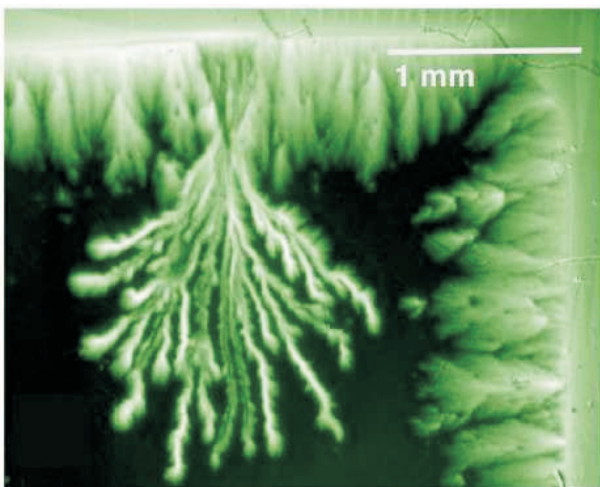

Fig. 2. Dendritic flux avalanche observed in MgB$_2$ film by MOI. From Ref. 6.
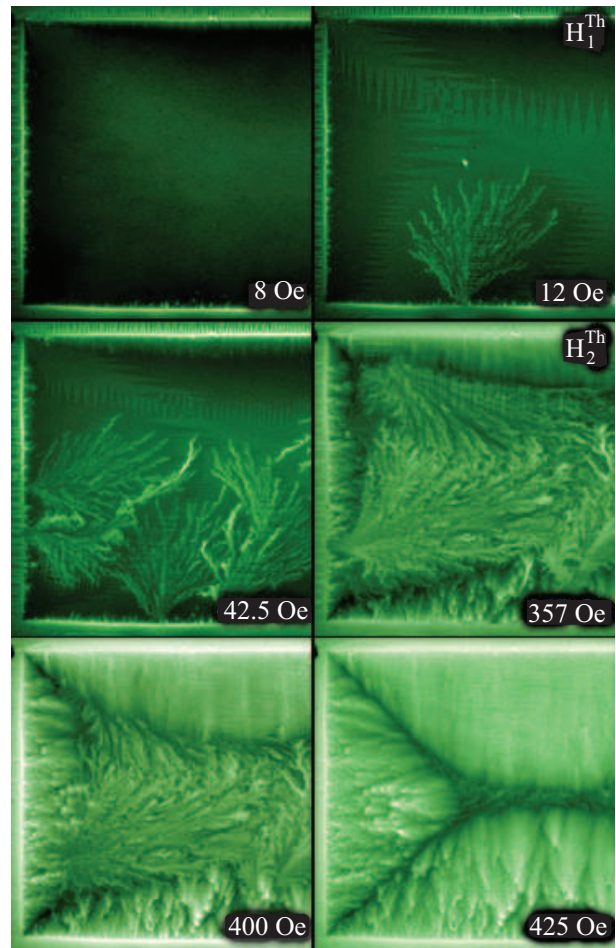

Fig. 3. Magneto-optical images of a NbN film at 4 K in increasing applied field illustrating development of the dendritic flux avalanches. From Ref. 24.

discovered that in most superconducting films, such as MgB$_2$, Nb, Pb, Nb$_3$Sn, NbN, YBa$_2$Cu$_3$O$_x$, and YNi$_2$B$_2$C, the avalanches create dendritic flux patterns (see Fig. 2) [6,11,12,17]. From the massive experimental data collected on the subject one can identify some common features of the dendritic instability:

(i) It occurs below a certain temperature T_{th} where $T_{th} < T_c$.

(ii) It occurs in a limited range of applied fields: $H_1^{th} \leq H \leq H_2^{th}$, where H_1^{th} and H_2^{th} are the so-called lower and upper threshold fields, respectively.

Shown in Fig. 3 is a set of images recorded during a slow ramping up of the applied magnetic field in a thin film of NbN after the sample was initially zero-field cooled to $T = 4$ K. In the image taken at $H = 8$ Oe, there is only a shallow penetration, with a flux front that gradually advanced during the field increase. This smooth mode of penetration ended abruptly when reaching $H = 12$ Oe, where a flux avalanche suddenly occurred. As the applied field increased further, more and more ava-

lanches took place, creating a complex pattern of flux dendrites covering most of the sample area, Fig. 3 ($H = 42.5$ Oe). Then, as the field reached $H = 357$ Oe, the avalanche activity stopped entirely although the field continued to increase. The advancing flux front now erased the previously formed dendritic structures, see images taken at $H = 400$ and 425 Oe, and the critical state mode of flux penetration was restored. The bright fan-like features in the lower part of the images are due to tiny film defects, and are not related to the flux instability.

(iii) The formation of the dendritic instability is a stochastic process.

Usually indentations on the sample edges serve as the most probable origins of the avalanches, as they give a significant local magnetic field amplification and increase in the electric field [26]. Nevertheless, the exact nucleation place of the next dendrite, field interval between two consecutive events, and the final shape of the dendritic structure are nonreproducible. To illustrate this, Fig. 4 shows three magneto-optical images of flux penetration in a MgB$_2$ film taken after three repeated experimental runs with initial zero-field-cooling the sample 9.2 K and applying a field of 20 mT. Image (*b*) was obtained by superimposing the three original images colored red, green, and blue, respectively. In those parts of the final image where they overlap, i.e., the flux front's behavior is reproducible, one observes a gradation of white. Different colors show the places where there is no overlap, or the overlap is only partial. Strong irreproducibility is seen in the dendrite shapes, while the penetration near the edge and along static defects is repeatable. Randomness in the behavior of the vortex matter also explains a large statistical variation of the measured $H_{1,2}^{th}$ values, which will be discussed later.
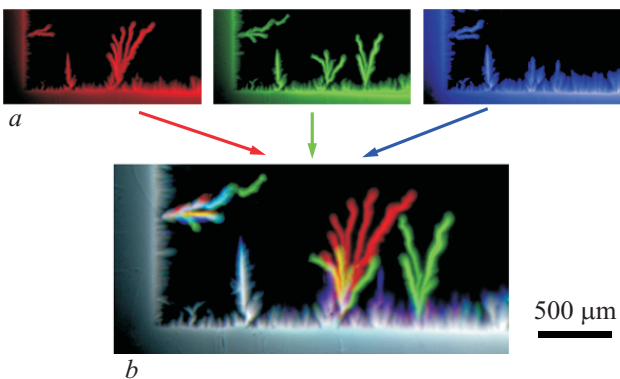

Fig. 4. MOI demonstrating irreproducibility of the flux distribution that results from the dendritic avalanches. (*a*) Three images were taken under identical experimental conditions. (*b*) Image obtained by superimposing the three images above. Repeatable parts of the flux front appear as gradations of white. From Ref. 25.
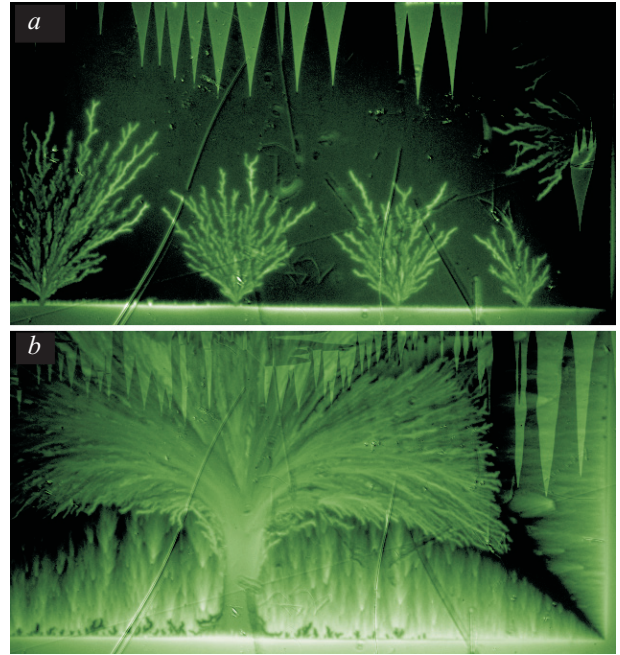

Fig. 5. Magneto-optical images of dendritic flux avalanches in a NbN film taken at *a*) $T = 4$ K and *b*) $T = 6$ K.

(iv) The degree of branching of the dendrites, sometimes represented by their fractal dimensionality, and size vary with temperature and the field.

Figure 5 illustrates typical behaviors of the dendrites in a NbN film at different temperatures. At $T = 4$ K the number of the dendritic avalanches per interval of the field was higher compared to $T = 6$ K. The size of the dendrites shows opposite trend — it increases when the temperature approached T_{th}. Regarding the dependences on magnetic field, at lower (slowly increasing) fields the avalanches are smaller in size, but appear in larger numbers per field interval. At larger fields, the dendrites are less frequent, but larger in size. Images in Fig. 3 taken at $H = 12$ and 357 Oe illustrate this property.

3. Theory of the dendritic flux jumps

There exist numerous experimental indications that the instability is a rather unavoidable generic feature of the vortex matter in superconductor thin films. The conventional theory of the thermomagnetic instability considered only «uniform» flux jumps, where the flux front is smooth and essentially straight [23,27]. The problem of the flux pattern formation was examined in the *slab* geometry [28] and more recently in thin films placed in perpendicular magnetic field [29,30]. The criteria for the instability onset were obtained from the linear analysis of small coordinate-dependent perturbations in the electric field, E, and temperature, T [25,31]. The problem was solved for a thin (thickness d is much less than the
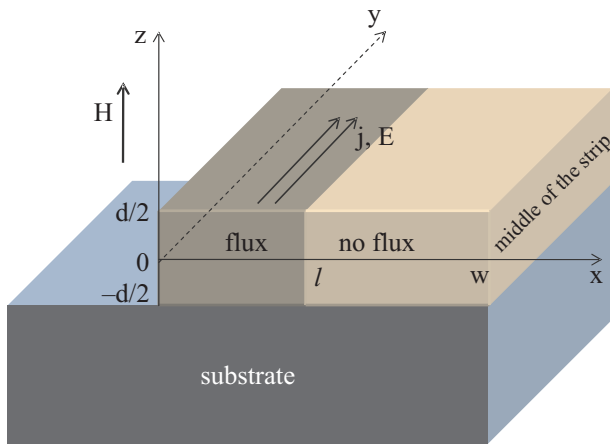
Fig. 6. One half of a superconductor strip on a substrate. The dark gray area is the flux-penetrated region (Ref. 31).

width $2w$) superconducting strip infinite in y direction, placed in a transverse magnetic field, **H**, and thermally coupled to the substrate (Fig. 6).

3.1. Model and basic equations

The thermomagnetic instability can be described by the set including the Maxwell equations and the equation for thermal conduction:

$$\text{curl } \mathbf{B} = \mu_0 \mathbf{j}, \tag{1}$$

$$\text{curl } \mathbf{E} = -\frac{\partial \mathbf{B}}{\partial t}, \tag{2}$$

$$C \frac{\partial T}{\partial t} = \kappa \nabla^2 T + \mathbf{j}\mathbf{E}. \tag{3}$$

In the above equations, **j** is the current density, **E** is the electric field, **B** is the magnetic induction, $\mathbf{B} = \mu_0 \mathbf{H}$; C is the specific heat, κ is the thermal conductivity. The heat release into substrate is taken into account by applying the boundary condition

$$\kappa \nabla_n T = -h_0 (T - T_0) \tag{4}$$

to both film surfaces. Here T_0 is temperature of the substrate, while h_0 characterizes heat transfer through the interface between the sample and the substrate. The above set should be supplemented by a relation between the current density, and the electric field, $j = j(E, B, T)$. This relation is chosen as

$$\mathbf{j} = j_c(T) g(E) (\mathbf{E}/E). \tag{5}$$

Here $g(E)$ represents a very steep $E(j)$ curve having large logarithmic derivative,

$$n(E) \equiv \partial \ln E / \partial \ln j \approx j_c / \sigma E \gg 1, \tag{6}$$

where σ is the differential electrical conductivity, $\sigma(E) \equiv \partial j / \partial E$. Parameter n stands for the exponent in the frequently used power-law relation $E \propto j^n$. A strong nonlinearity of the function $g(E)$ leads to a formation of a quasistatic critical state with $j \approx j_c(T)$, where j_c is the critical current density. Note that in this model B-dependence of j_c is neglected, as in the Bean's model [5]. We will come back to this assumption later.

The key dimensionless parameter of the model is the ratio of the thermal and magnetic diffusion coefficients [23],

$$\tau \equiv \mu_0 \kappa \sigma / C. \tag{7}$$

The smaller is τ, the slower heat diffuses from the perturbation region into the surrounding areas. Hence, one can expect that for smaller τ the superconductor is more unstable, and the formation of instability-induced nonuniform structures is more likely. Solutions of Eqs. (1)–(5) were sought within linear perturbation analysis in the form

$$T + \delta T(x, y, z, t), \quad \mathbf{E} + \delta \mathbf{E}(x, y, z, t), \quad \mathbf{j} + \delta \mathbf{j}(x, y, z, t)$$

with perturbations $\delta T, \delta E_{x,y}$, and $\delta j_{x,y}$ determined via corresponding dimensionless Fourier amplitudes θ, ε, and i:

$$\delta T = T^* \theta \exp(\lambda t / t_0 + i k_x \xi + i k_y \eta),$$

$$\delta E_{x,y} = E \varepsilon_{x,y} \exp(\lambda t / t_0 + i k_x \xi + i k_y \eta),$$

$$\delta j_{x,y} = j_c i_{x,y} \exp(\lambda t / t_0 + i k_x \xi + i k_y \eta). \tag{8}$$

These components can be regarded as z-independent for a thick slab. For the case of a thin film they should be properly averaged over z, see Ref. 31 for details.

3.2. Criteria for dendritic instability in thin films

Here we will focus on the analysis of the main results of Ref. 31. Provided there exists a set of parameters that satisfies $\text{Re } \lambda(k_x, k_y) > 0$, the superconductor becomes unstable. The wave vectors k_x and k_y characterize the extent of the flux front perturbations in corresponding directions. Instability would develop to a fingering pattern if $k_x \ll k_y \neq 0$. The critical k_y^* and k_x^* for the fingering instability can be found from the requirement $\max\{\text{Re } \lambda(k_y)\} = 0$ for $k_y \neq 0$ in the limit $d/2l \ll 1$ (notations follow from Fig. 6):

$$k_x^* = \frac{\sqrt{n+1} - \sqrt{nh\tau}}{n\sqrt{\tau}},$$

$$k_y^* = \frac{(nh\tau + 1)^{1/4} (\sqrt{n+1} - \sqrt{nh\tau + 1})^{1/2}}{\sqrt{n\tau}},$$

$$h \equiv \frac{2h_0 C}{\mu_0 j_c^2 \kappa d (\partial \ln j_c / \partial T)}. \tag{9}$$

Since the front penetration depth, l, is related to the applied field according to Ref. 32, the quantity $k_x^* \propto 1/l$ determines the applied magnetic field at which the instability first takes place. The quantity k_y^* determines spatial scale of the fingers. Dispersion relations Re $\lambda(k_x, k_y)$ for arbitrary k_y are presented in Fig. 7. For small τ and large k_x, i.e., small magnetic field, Re λ is negative for all k_y (Fig. 7,a), meaning the superconductor is stable. At small k_x, Re λ becomes positive in some finite range of k_y, which implies that perturbations with finger patterns of elevated T and E will start growing perpendicular to the flux front, giving rise to the *dendritic instability*. For large τ, i.e., large heat diffusion, at small k_x the maximum of Re λ corresponds to $k_y = 0$, and the uniform perturbation will be dominant (Fig. 7,b).

One of the most important results that can be directly tested in experiments is the threshold flux penetration depth l^*, when the superconductor becomes unstable [25]. Putting in Eqs. (9) $l^* = 1/k_y^*$ one obtains:

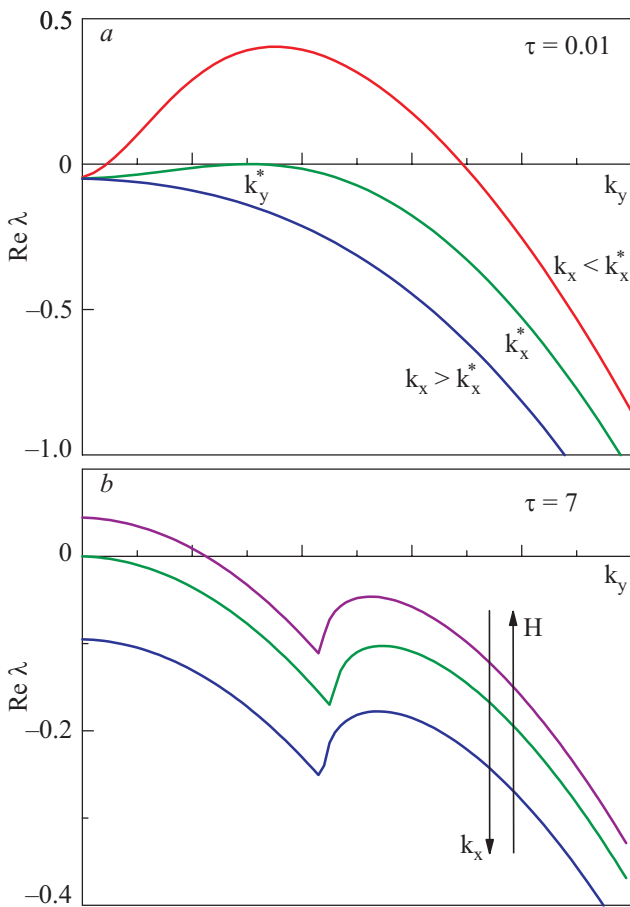$$l^* = \frac{\pi}{2}\sqrt{\frac{\kappa}{|j_c'|E}}\left(1 - \sqrt{\frac{2h_0}{nd|j_c'|E}}\right)^{-1}. \tag{10}$$

Here j_c' is the temperature derivative of the critical current density. By combining Eq. (10) with the Bean model expression for the flux penetration depth of a thin superconducting strip in transverse field [32] one immediately arrives at the expression for the threshold field:

$$H_{th} = \frac{j_c d}{\pi}\,\mathrm{arccosh}\left(\frac{w}{w - l^*}\right). \tag{11}$$

Equations (10), (11) set the most practically important relations between the external parameters, such as the field and temperature, on one hand, and the sample properties (κ, h_0, j_c, w) on the other. In order to check the validity of the model, the threshold field was measured first in a series of MgB$_2$ samples of different width. A set of eight thin film samples was deposited in one run to allow
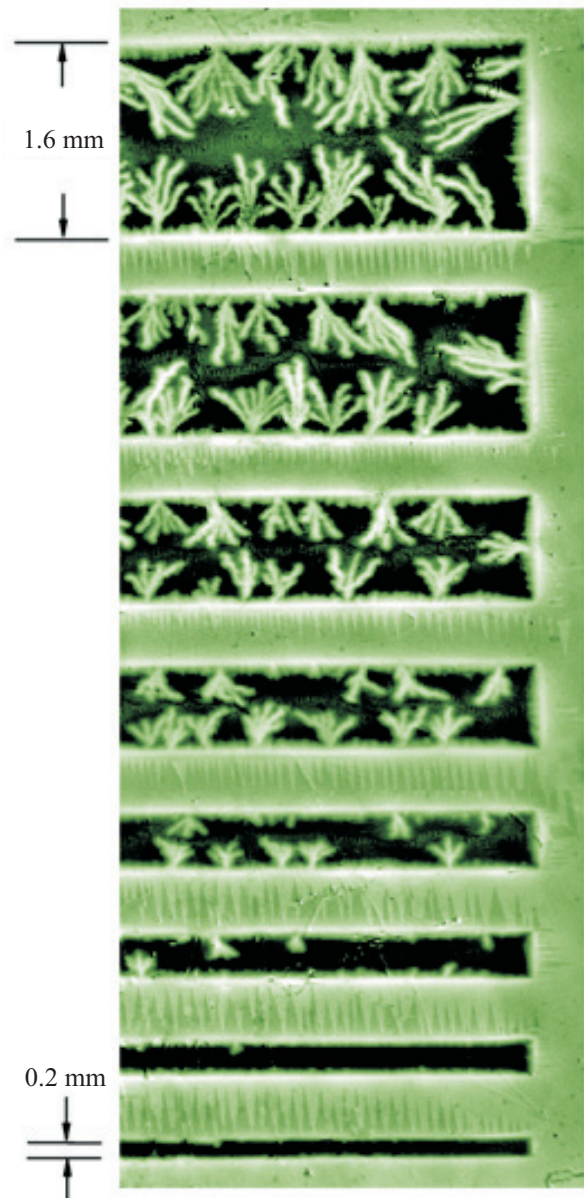

Fig. 7. Dispersion relations Re $\lambda(k_x, k_y)$ for small and large τ, for $d/2l = 0.001$ and $n = 20$. From Ref. 31.

Fig. 8. MOI of flux distribution in MgB$_2$ samples of different width at 4 K and magnetic field of 15 mT. From Ref. 25.
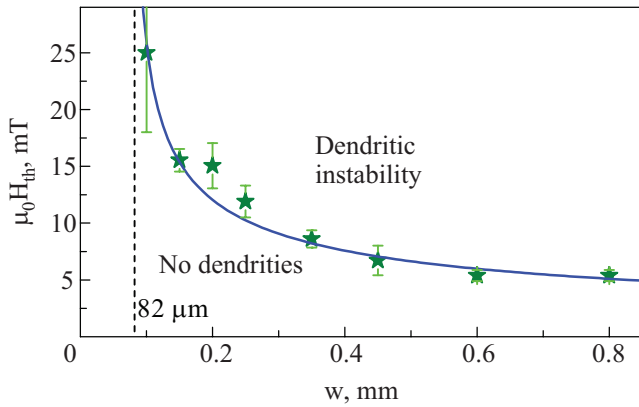
Fig. 9. Threshold magnetic field for onset of the dendritic instability in MgB$_2$ strips of different width. Experimental data (symbols) are in a good agreement with a fitted theoretical curve (full line), for $j_c = 0.9 \cdot 10^{11}$ A/m^2. From Ref. 25.

for a direct comparative analysis and shaped later by photolithography into 3 mm long rectangles having different widths ranging from 0.2 to 1.6 mm. In Fig. 8 presenting the results of MOI experiments, the dendrites pronouncedly invade the wider strips, while there are fewer of them in the samples with smaller widths, and no dendrites at all in the one with $w = 0.2$ mm. The quantitative results for $H_{th}(w)$ are summarized in Fig. 9. The fitted data reproduce the experimentally observed tendency of the threshold field to diverge as the strip becomes narrower. Rephrasing the latter statement, the narrower is the superconductor the more thermomagnetically stable it is.

A good agreement between the theory and experiment was also obtained for the threshold field as a function of temperature. To fit the $H_{th}(T)$, observed in Nb and MgB$_2$
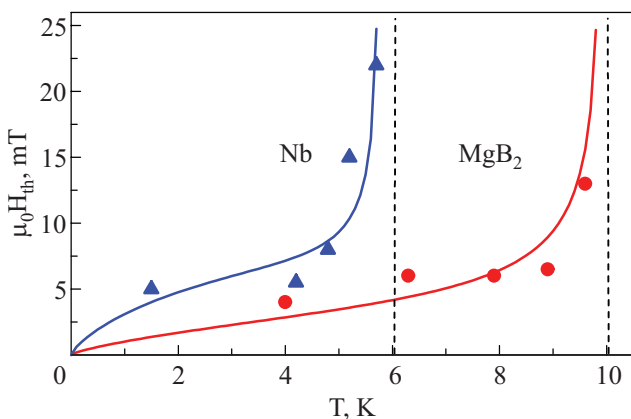

Fig. 10. Temperature dependence of the threshold magnetic field (from Ref. 25). Experimental data obtained for the 5 mm wide MgB$_2$ sample (●) and for a 1.8 mm wide Nb film (▲) [13]. The full lines are theoretical fits. The dashed lines show the limiting temperature above which the instability vanishes.

thin films (Fig. 10), some assumptions for temperature dependent model parameters had to be made. The assumed cubic dependencies for the thermal conductivity, $\kappa = \widetilde{\kappa}(T/T_c)^3$, and the heat transfer coefficient, $h_0 = \widetilde{h}_0(T/T_c)^3$, were based on the low-temperature data for MgB$_2$ [33] and the acoustic mismatch model [34], respectively. The critical current density was assumed to depend linearly on temperature: $j_c = j_{c0}(1 - T/T_c)$. Given a pinning potential, $U \propto (1 - T/T_c)$, the exponent $n \sim U/kT$ becomes T-dependent, $n = \widetilde{n}(T_c/T - 1)$. The model clearly reproduces the property (i) mentioned above — existence of a threshold temperature T_{th} such that for $T > T_{th}$ the instability is absent, and a steep increase of the threshold field H_{th} when T approaches T_{th}.

4. Reentrant stability of superconducting films

Although the existence of the lower threshold magnetic field, H_1^{th}, was explained in Sec. 3, the origin of the upper threshold field, H_2^{th}, above which the flux distributions are stable, was not discussed. Recently, we managed to put the existence of an upper threshold into the framework of the model described in the previous section [24].

As it follows from Eqs. (10) and (11), the threshold field depends nonmonotonously on the critical current density, as shown in Fig. 11. For intermediate j_c the threshold field is nearly constant, and increases slowly as j_c becomes larger giving eventually a sublinear asymptotic dependence, $H_{th} \sim j_c^{3/4}$. More importantly, when j_c decreases the threshold field diverges at some finite j_c,
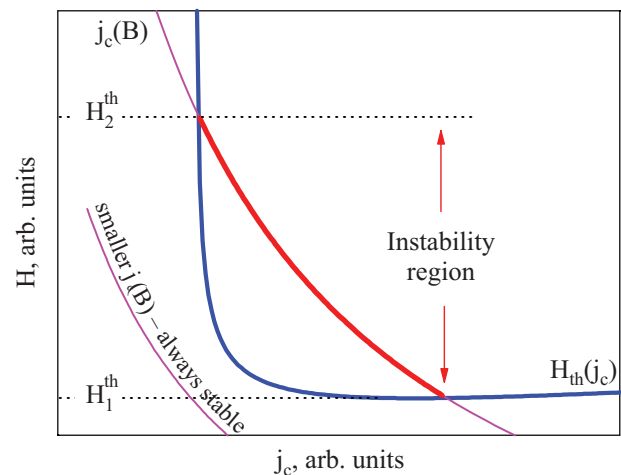

Fig. 11. Schematic plot illustrating the existence of two threshold fields for the dendritic instability adapted from Ref. 24. The two main curves represent dependencies of the threshold filed on the critical current density $H_{th}(j_c)$ and a typical monotonous field dependence of j_c. The intersection of the two curves defines the two thresholds H_1^{th} and H_2^{th} for the onset and vanishing of the instability.

corresponding to $l^*(j_c)$ approaching w. Taking into account that the critical current density most commonly decreases with the field, it follows that the field range with unstable behavior can indeed have both a lower and upper limit, H_1^{th} and H_2^{th}, as indicated in the figure. Evidently, it is essential how fast j_c is decreasing with the field. In particular, along the Bean model (constant j_c), or with a j_c having only weak field dependence, the conditions for having an upper threshold will never be met. Note also that if j_c is sufficiently small, e.g., because of a larger temperature, the thermomagnetic avalanches will not occur at any magnetic field.

This idea was supported by MOI experiments on a NbN superconductor thin film. To measure both j_c and the upper and lower instability threshold fields the sample was field-cooled to 4 K in various constant magnetic fields, H_{fc}. The field-dependent critical current density $j_c(H_{fc})$ was determined from the depth of the penetration front in the middle section of the rectangular sample [32,35]. A nearly exponential decay was found, with j_c decreasing from $7.6\cdot10^{10}$ A/m^2 at zero field to almost one half at $H_{fc} = 300$ Oe, which agrees well with the results obtained earlier from ac susceptibility measurements [36] on the same type of films. The threshold fields were determined by slowly ramping up the additional field after an initial field-cooling in extern field H_{fc}. Figures 12 and 13 present the experimentally obtained functions $j_c(H_{fc})$ and $H_{1,2}^{th}(H_{fc})$, which were used to make the parametric plot of the instability onset field $\Delta H = H_1^{th} - H_{fc}$ shown in Fig. 14. Note that under field-cooling the vortices are distributed homogeneously inside this superconductor where pinning is fairly strong.

Application of additional field leads to a build-up of the critical state, which collapses due to the thermomagnetic instability as soon as the flux front advances over
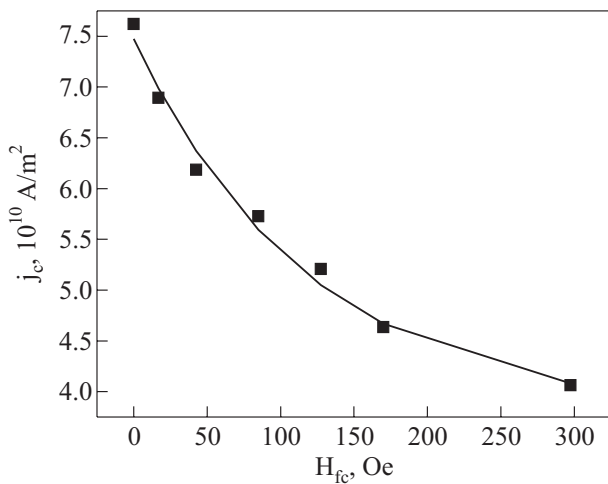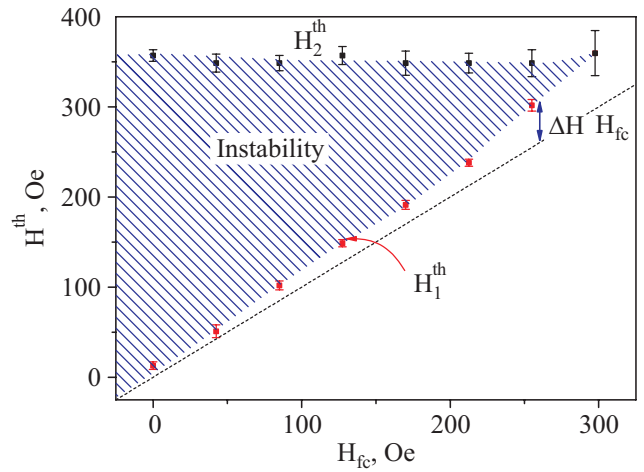

Fig. 13. Thermomagnetic instability diagram of NbN at $T = 4$ K (Ref. 24): the lower and upper threshold fields H_1^{th} and H_2^{th}, measured at different H_{fc}, limit the region where the dendritic avalanches were observed.

the threshold length l^* corresponding to applying the additional field ΔH. Figure 14 demonstrates an excellent quantitative agreement between the experimental data for NbN (symbols) and theoretical curve obtained from Eqs. (10) and (11), using only two fitting parameters, $\kappa T_{th}/E = 500$ mA and $h_0 T_{th}/nE = 5700$ A/m (these parameter values can be achieved, e.g., with the combination $\kappa = 25$ mW/(K·m), $h_0 = 1424$ W/(K·m^2), $n = 5$, $E = 0.55$ V/m, $T_{th} = 11$ K). As mentioned above, the dendrite formation process is stochastic, which is reflected in a noticeable dispersion of the measured threshold fields and the error bars in the figures, calculated as a standard deviation for repeated experiments.
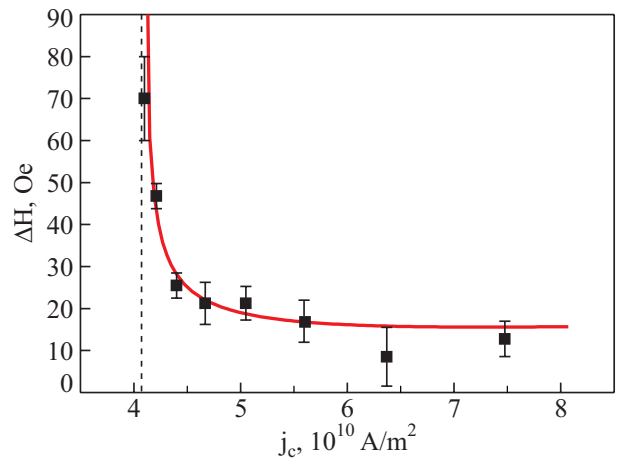

Fig. 12. Field dependence of the critical current density at $T = 4$ K measured using MOI in NbN thin film (Ref. 24).

Fig. 14. Instability onset field ΔH as a function of the critical current at 4 K in NbN thin film. From Ref. 24.

5. Summary and conclusions

In this work, we review both well established facts and the results of very recent experiments on dendritic instabilities in superconductor films. The most common properties of the dendritic instability are summarized in Sec. 2. In Sec. 3 we introduced the recent theoretical model allowing to understand key features of the instability and link them to the samples' parameters. These links are provided by Eqs. (10) and (11) for the threshold field H_{th} as a function of temperature, the critical current density j_c, the sample width w, the thermal conductivity κ. It was demonstrated that the model explains the observed reentrant behavior of the dendritic instability and allows to quantify its upper and lower critical fields. The validity of the model is illustrated by several experiments confirming its predictions.

Acknowledgments

1. A.A. Abrikosov, *Sov. Phys. JETP* **5**, 1174 (1957).
2. G. Blatter, M.V. Feigel'man, V.B. Geshkenbein, A.I. Larkin, and V.M. Vinokur, *Rev. Mod. Phys.* **66**, 1125 (1994).
3. E.H. Brandt, *Rep. Prog. Phys.* **58**, 1465 (1995).
4. R. Wördenweber, *Rep. Prog. Phys.* **62** 187 (1999).
5. C.P. Bean, *Rev. Mod. Phys.* **36**, 31 (1964).
6. T.H. Johansen, M. Baziljevich, D.V. Shantsev, P.E. Goa, Y.M. Galperin, W.N. Kang, H.J. Kim, E.M. Choi, M.-S. Kim, and S.I. Lee, *Europhys. Lett.* **59**, 599 (2002).
7. F.L. Barkov, D.V. Shantsev, T.H. Johansen, P.E. Goa, W.N. Kang, H.J. Kim, E.M. Choi, and S.I. Lee, *Phys. Rev.* **B67**, 064513 (2003).
8. Z.X. Ye, Q. Li, Y.F. Hu, A.V. Pogrebnyakov, Y. Cui, X.X. Xi, J.M. Redwing, and Q. Li, *Appl. Phys. Lett.* **85**, 5284 (2004).
9. J. Albrecht, A.T. Matveev, M. Djupmyr, G. Schütz, B. Stuhlhofer, and H.-U. Habermeier, *Appl. Phys. Lett.* **87**, 182501 (2005).
10. F. Laviano, D. Botta, C. Ferdeghini, V. Ferrando, L. Gozzelino, and E. Mezzetti, in: *Magneto-Optical Imaging*, T.H. Johansen and D. Shantsev (eds.), Kluwer Academic (2004), p. 237.
11. M.R. Wertheimer and J. de G. Gilchrist, *J. Phys. Chem. Solids* **28**, 2509 (1967).
12. C.A. Duran, P.L. Gammel, R.E. Miller, and D.J. Bishop, *Phys. Rev.* **B52**, 75 (1995).
13. M.S. Welling, R.J. Westerwaal, W. Lohstroh, and R.J. Wijngaarden, *Physica* **C411**, 11 (2004).
14. M. Menghini, R.J. Wijngaarden, A.V. Silhanek, S. Raedts, and V.V. Moshchalkov, *Phys. Rev.* **B71**, 104506 (2005).
15. I.A. Rudnev, S.V. Antonenko, D.V. Shantsev, T.H. Johansen, and A.E. Primenko, *Cryogenics* **43**, 663 (2003).
16. I.A. Rudnev, D.V. Shantsev, T.H. Johansen, and A.E. Primenko, *Appl. Phys. Lett.* **87**, 042502 (2005).
17. P. Leiderer, J. Boneberg, P. Brull, V. Bujok, and S. Herminghaus, *Phys. Rev. Lett.* **71**, 2646 (1993).
18. B. Biehler, B.-U. Runge, P. Leiderer, and R.G. Mints, *Phys. Rev.* **B72**, 024532 (2005).
19. S.C. Wimbush, B. Holzapfel, and Ch. Jooss, *J. Appl. Phys.* **96**, 3589 (2004).
20. E. Altshuler and T.H. Johansen, *Rev. Mod. Phys.* **76**, 471 (2004) and references therein.
21. S.J. Bending, *Adv. Phys.* **48**, 449 (1999).
22. M.R. Koblischka and R.W. Wijngaarden, *Supercond. Sci. Technol.* **8**, 199 (1995).
23. R.G. Mints and A.L. Rakhmanov, *Rev. Mod. Phys.* **53**, 551 (1981).
24. V.V. Yurchenko, D.V. Shantsev, T.H. Johansen, M.R. Nevala, I.J. Maasilta, K. Senapati, and R.C. Budhani, *Phys. Rev.* **B76**, 092504 (2007).
25. D.V. Denisov, D.V. Shantsev, Y.M. Galperin, E.-M. Choi, H.-S. Lee, S.-Ik Lee, A.V. Bobyl, P.E. Goa, A.A.F. Olsen, and T.H. Johansen, *Phys. Rev. Lett.* **97**, 077002 (2006).
26. J.I. Vestgaarden, D.V. Shantsev, Y.M. Galperin, and T.H. Johansen, *Phys. Rev.* **B76**, 174509 (2007).
27. A.Vl. Gurevich, R.G. Mints, and A.L. Rakhmanov, *The Physics of Composite Superconductors*, Begell House Inc., NY (1997). In Russian: A.Vl. Gurevich, R.G. Mints, and A.L. Rakhmanov, *The Physics of Composite Superconductors*, Science, Moscow (1987).
28. A.L. Rakhmanov, D.V. Shantsev, Y.M. Galperin, and T.H. Johansen, *Phys. Rev.* **B70**, 224502 (2004).
29. I.S. Aranson, A. Gurevich, M.S. Welling, R.J. Wijngaarden, V.K. Vlasko-Vlasov, V.M. Vinokur, and U. Welp, *Phys. Rev. Lett.* **94**, 037002 (2005).
30. C. Baggio, R.E. Goldstein, A.I. Pesci, and W. van Saarloos, *Phys. Rev.* **B72**, 060503 (2005).
31. D.V. Denisov, A.L. Rakhmanov, D.V. Shantsev, Y.M. Galperin, and T.H. Johansen, *Phys. Rev.* **B73**, 014512 (2006).
32. E.H. Brandt and M. Indenbom, *Phys. Rev.* **B48**, 12893 (1993).
33. M. Schneider, D. Lipp, A. Gladun, P. Zahn, A. Handstein, G. Fuchs, S. Drechsler, M. Ritcher, K. Muller, and H. Rosner, *Physica* **C363**, 3 (2001).
34. E.T. Swartz and R.O. Pohl, *Rev. Mod. Phys.* **61**, 605 (1989).
35. A more precise way to determine $j_c(B)$ should be based on the self-consistent relation between the depth of the flux front and the $j_c(B)$ law derived in J. McDonald and J.R. Clem, *Phys. Rev.* **B53**, 8643 (1996).
36. K. Senapati, N.K. Pandey, R. Nagar, and R.C. Budhani, *Phys. Rev.* **B74**, 104514 (2006).